Electromagnetic constraints on a melt region beneath the central Mariana back-arc spreading ridge

Tetsuo Matsuno
Department of Earth and Planetary Sciences, Kobe University, 1–1 Rokkodai, Nada, Kobe 657–8501, Japan (tmatsuno@pony.kobe–u.ac.jp)

Rob L. Evans
Department of Geology and Geophysics, Woods Hole Oceanographic Institution, Woods Hole, Massachusetts 02543, USA (revans@whoi.edu)

Nobukazu Seama
Department of Earth and Planetary Sciences, Kobe University, 1–1 Rokkodai, Nada, Kobe 657–8501, Japan (seama@kobe–u.ac.jp)

Alan D. Chave
Department of Applied Ocean Physics and Engineering, Woods Hole Oceanographic Institution, Woods Hole, Massachusetts 02543, USA (achave@whoi.edu)

[1] An electrical resistivity profile across the central Mariana subduction system shows high resistivity in the upper mantle beneath the back-arc spreading ridge where melt might be expected to exist. Although seismic data are equivocal on the extent of a possible melt region, the question arises as to why a 2-D magnetotelluric (MT) survey apparently failed to image any melt. We have run forward models and inversions that test possible 3-D melt geometries that are consistent with the MT data and results of other studies from the region, and that we use to place upper bounds on the possible extent of 3-D melt region beneath the spreading center. Our study suggests that the largest melt region that was not directly imaged by the 2-D MT data, but that is compatible with the observations as well as the likely effects of melt focusing, has a 3-D shape on a ridge-segment scale focused toward the spreading center and a resistivity of 100 Ω-m that corresponds to $\sim$0.1–$\sim$1% interconnected silicate melt embedded in a background resistivity of $\sim$500 Ω-m. In contrast to the superfast spreading southern East Pacific Rise, the 3-D melt region suggests that buoyant mantle upwelling on a ridge-segment scale is the dominant process beneath the slow-spreading central Mariana back-arc. A final test considers whether the inability to image a 3-D melt region was a result of the 2-D survey geometry. The result reveals that the 2-D transect completed is useful to elucidate a broad range of 3-D melt bodies.

1. Introduction

[2] Recent geophysical experiments at the central Mariana subduction system have imaged the upper mantle in some detail [*Matsuno et al.*, 2010; *Pozgay et al.*, 2009; *Pyle et al.*, 2010; *Barklage*, 2010]. In particular, a large magnetotelluric (MT) study determined the electrical resistivity structure of the mantle along a transect extending from the incoming Pacific plate across the trench and the arc, and crossing the 18°S segment of the back-arc spreading center [*Matsuno et al.*, 2010] (Figure 1). The electrical resistivity structure of the mantle is sensitive to temperature, the presence of water in olivine and especially to the presence of a small volume of interconnected melt phases, and hence MT methods provide an ideal complement to seismic approaches for imaging the mantle. The model produced from the MT data contains a large conductive feature associated with dehydration-driven melting of the mantle above the downgoing slab. However, a particularly striking result is the lack of evidence for enhanced electrical conductivity that would infer the presence of melt beneath the back arc spreading center (Figure 1), in apparent contradiction to the result for seismic attenuation [*Pozgay et al.*, 2009]. This outcome led us to question whether some melt could be present in the upper mantle beneath the spreading center, but located in a region of such limited spatial extent that it remained undetected. The purposes of this paper are addressing this question and exploring a range of plausible melt regions with the aim of bounding the melt column dimensions.

[3] Possible explanations for high resistivity in the mantle beneath the spreading center are that no more than a small amount of melt that is poorly interconnected is present within the mantle, or that the slow spreading ridge system results in 3-D melt delivery with a limited along-strike dimension that is difficult to image with data collected along a 2-D transect [*Matsuno et al.*, 2010]. The slow spreading rate of the ridge would lead us to prefer the second explanation, as other observations at slow spreading centers predict segmented melt delivery to the ridge crest [e.g., *Lin et al.*, 1990; *Forsyth*, 1996].

[4] Seismological images of the mantle beneath the Marianas system similarly fail to conclusively image a melt body. Seismic attenuation is generally high, suggesting the existence of <1% melt in a columnar shape with a width of ∼75 km down to ∼100 km depth [*Pozgay et al.*, 2009]. 3-D body wave tomography shows that seismic velocities (both Vp and Vs) are low beneath the spreading center, and that the Vp/Vs ratio is moderately high beneath the spreading ridge but is lower than that beneath the arc [*Barklage*, 2010]. These anomalies suggest the existence of a small amount of melt and/or water, but they are also compatible with expected thermal variations in the upper mantle and also with variations in the grain size of polycrystalline olivine [*Barklage*, 2010]. The shear velocity structure inferred from Rayleigh wave phase velocity contains slightly slow values that are shifted trenchward from the spreading center [*Pyle et al.*, 2010].

[5] The back-arc spreading segment that the electromagnetic and seismic transects cross has a slow spreading rate of ∼30 mm/yr [e.g., *Bibee et al.*, 1980; *Kato et al.*, 2003], similar to the spreading rate of the whole Mariana back-arc ridge [e.g., *Hussong and Uyeda*, 1982]. The length of the segment is ∼60 km, and the topography of the segment has features typical of a slow spreading system, with a median valley and a topographic high at the segment center [e.g., *Kitada et al.*, 2006]. Analysis of gravity data shows a circular mantle Bouguer anomaly low beneath the target segment, a smaller low anomaly beneath the adjacent segment to the south, and no anomaly beneath the adjacent segment to the north [*Kitada et al.*, 2006]. A reflection and refraction seismic survey across a segment exhibiting a similar gravity signature as for the MT transect [*Kitada et al.*, 2006] shows thickening of the crust and deep reflectors near the top of the upper mantle just beneath the spreading center [*Takahashi et al.*, 2008]. These deep reflectors might indicate the existence of low velocity material including melt [*Takahashi et al.*, 2008].

[6] Geochemical mapping along the Mariana back-arc spreading ridge indicates that there is locally focused mantle upwelling beneath a few segments where MORB-like composition is dominant [*Pearce et al.*, 2005; *Pearce and Stern*, 2006]. The location of one of the upwelling regions predicted by Pearce *et al.* is near the target segment of the electromagnetic and seismic experiments. Hydration of the source
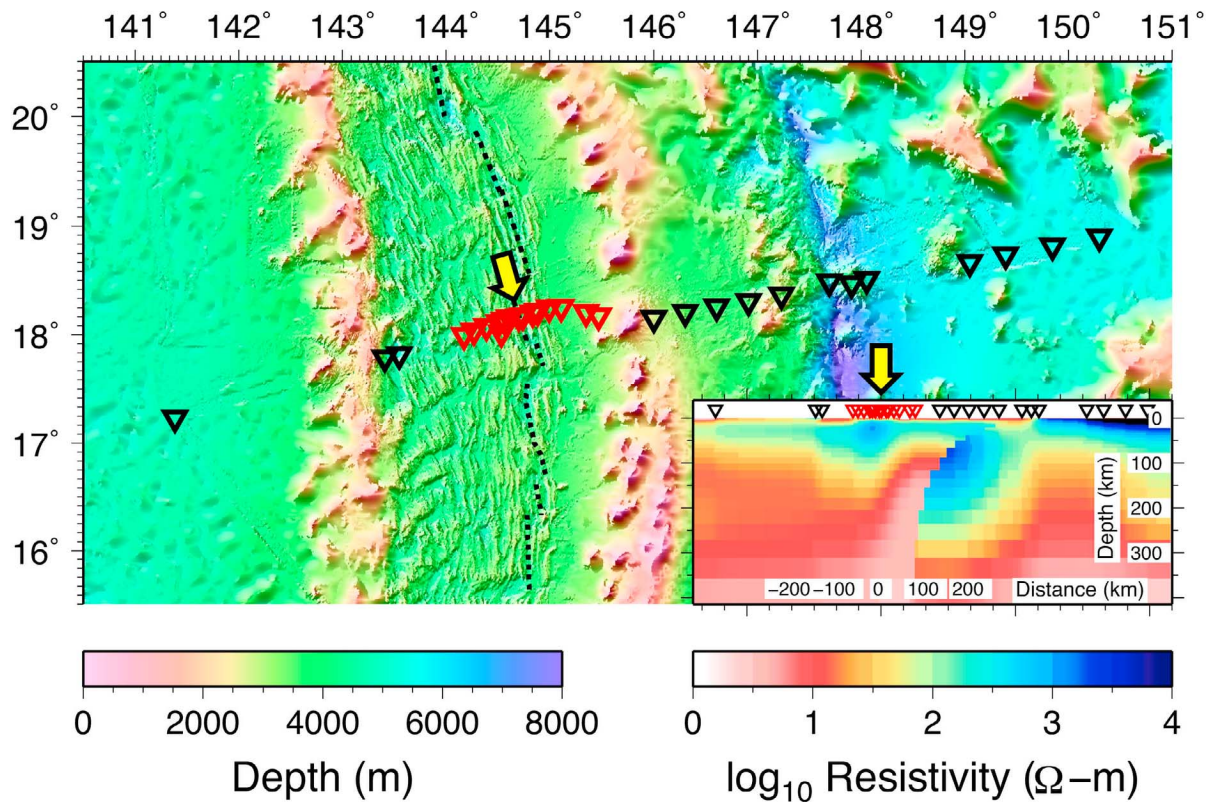
Figure 1. A bathymetric map of the central Marianas with the MT site locations (inverted triangles) and the optimal 2-D inversion model of *Matsuno et al.* [2010] in the inset. The observed data at all of the inverted triangles were used in the inversions of *Matsuno et al.* [2010]. Data at the red inverted triangles located within 80 km of the spreading center are considered in the forward modeling test, and are replaced with synthetic data for the inversion test. Data at the black triangles are also used in the inversion test. Yellow arrows indicate the axis of the back-arc spreading. Dashed lines in the bathymetric map show the location of the back-arc spreading axis in the Mariana Trough [*Kitada et al.*, 2006].

mantle was revealed by analyses of petrological samples from the Mariana back-arc spreading ridge [e.g., *Stolper and Newman*, 1994; *Kelley et al.*, 2006], and this hydration could trigger melting at increased depth. *Hawkins et al.* [1990] showed that the axial ridge of the central Mariana has petrologic segmentation coincident with tectonic/morphologic segmentation, suggesting the existence of localized magma chambers and/or variations in the mantle source over length scales comparable to those of ridge segmentation.

[7] Observations at the Mid-Atlantic Ridge (MAR) suggest that mantle melt regions have a 3-D geometry, lending further evidence to the idea that melt delivery is segmented at slow spreading centers. Mantle Bouguer anomalies beneath segments between 33 and 35°N display circular lows, and numerical simulations of them support 3-D mantle flow to segment centers from a deeper mantle

source region [e.g., *Lin et al.*, 1990; *Magde et al.*, 1997]. Integrated analysis of active-source seismic survey data at one of the segments displays the signature of melt focusing toward the segment center both along- and across-strike in the crust and the uppermost mantle [*Dunn et al.*, 2005]. Tele-seismic PKP-phase tomography at another segment of the MAR reveals rapid variation in travel time extending away from the ridge axis, suggesting a narrow melt region with a large melt fraction (<5%) formed by dynamic upwelling or by veins and dikes, resulting in a narrow transport zone [*Forsyth*, 1996].

[8] In terms of electrical resistivity structures at slow spreading ridge systems, although 2-D and 3-D images for melt regions are generally lacking, a few 1-D depth profiles have failed to show conductive features. Magnetotelluric sounding at an axial volcanic ridge at the Reykjanes Ridge [*Heinson et al.*,
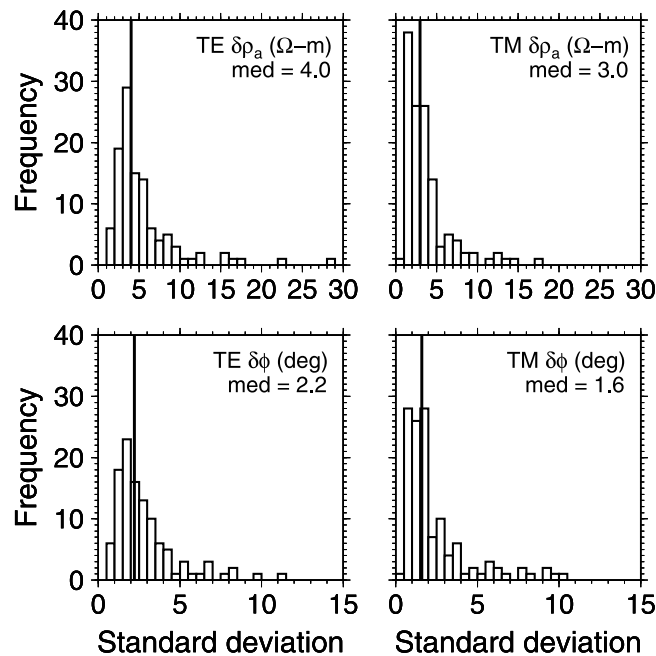
Figure 2. Histograms of the observed standard deviation for a subset of the data that were used in the 2-D optimal inversions of *Matsuno et al.* [2010]. The subset includes observational sites within 80 km on either side of the spreading center (the red triangles in Figure 1). The vertical line indicates the median of the standard deviation for each element that is used to normalize the residuals at hypothetical data points. The standard deviation of apparent resistivity in the TE mode is shown only for reference because this element was not used by *Matsuno et al.* [2010] or in this study.

2000] showed a resistivity of 100–200 Ω-m at depths shallower than 40 km, leading to the conclusion that an insignificant melt fraction is retained at these depths and that melt supply to a mid-crustal magma chamber, imaged by a controlled source electromagnetic survey [*MacGregor et al.*, 1998], is episodic. The electrical resistivity structure beneath another back-arc ridge segment in the Mariana Trough has a resistivity of 100–300 Ω-m at depths shallower than ~200 km [*Seama et al.*, 2007], suggesting a small melt fraction and/or a 3-D shaped melt region similar to the observations from the central Marianas.

2. Method and Melt Region Models

[9] Melt regions that are consistent with the MT data from the central Marianas were investigated through a series of electromagnetic forward modeling and inversion tests using synthetic forward responses. Synthetic data generated from electrical resistivity models in which 3-D conductive anomalies representing possible melt regions are superimposed are used in both types of test. The FS3D forward modeling program [*Baba and Seama*, 2002] was used to generate the synthetic data for the models. The forward and inversion

models include a flat seafloor of 4 km depth. The numerical gridding used in the 3-D forward modeling is different from that used in *Matsuno et al.* [2010], while that used in the 2-D inversion in this study is consistent with that used in *Matsuno et al.* [2010]. In the forward modeling test, the basic 2-D model is slightly modified from the optimal 2-D model [*Matsuno et al.*, 2010, Figure 6c] to remove small-scale artifacts in the upper 6 km that result from the lack of data sensitive to crustal structure. This change prevents numerical instability from occurring during forward modeling.

[10] In the forward modeling test, the size of the residuals (the differences between the responses for the model being tested and the background model) is used to decide whether the result is statistically compatible within the experimental error, and hence whether the tested melt region is acceptable or not. The residual is normalized by the experimental error (i.e., observed standard deviation) at each observational data point (i.e., at each site and at each frequency), and is defined by $(F(\mathbf{m}_{test}) - F(\mathbf{m}_{background}))/\sigma$, where $F(\mathbf{m})$ is a modeled value using the parameters either of $\mathbf{m}_{test}$ (tested model) or $\mathbf{m}_{background}$ (background model) through a forward modeling operator F, and σ is the observed standard deviation. A tested melt region model is
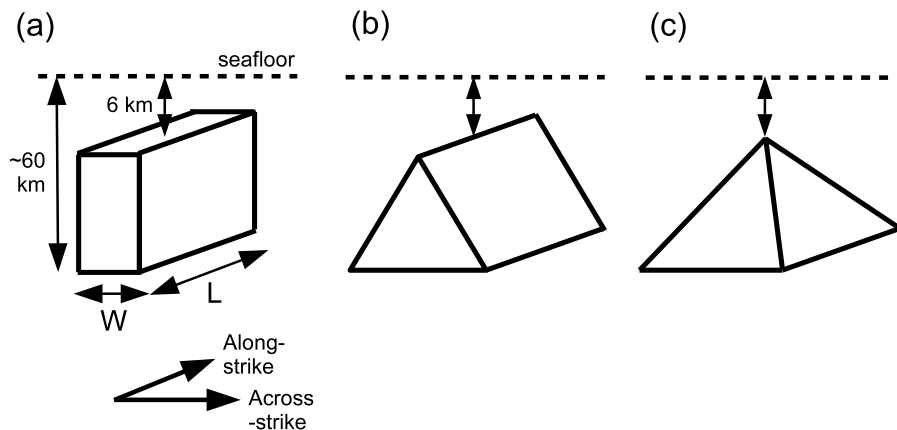
Figure 3. Cartoons showing (a) rectangular column, (b) triangular, and (c) pyramidal melt region models considered in the present study.

accepted when the absolute values of the normalized residuals are less than 1, and is rejected when any of the absolute values of normalized residuals at the observational data points are larger than 1. However, there is scatter in the size of the observed standard deviations, and we consider additional residuals at hypothetical data points to confirm the difference between the two synthetic data sets. These additional residuals at the hypothetical data points, which are not necessarily coincident with the observational data points, are normalized by the median of the observed standard deviation. The median is a good representation of the observed standard deviations (Figure 2). The data points considered in the analysis are located within 80 km on either side of the back-arc spreading center because sites beyond this range are not strongly influenced by the existence or the non-existence of a melt body beneath the spreading center. The number of discrete seafloor sites considered is 12, and are coincident with site numbers 4–15 in *Matsuno et al.* [2010]. The minimum period considered is 10^3 s, consistent with the minimum period reliably measured during the Marianas MT experiment. This choice of minimum period impacts our conclusions below, as some models show differences in MT responses in the band from 10^2-10^3 s. The inability to record shorter periods was the result of a weak source signal due to the experiment taking place during a solar minimum and the deep water in which the instruments were deployed (the average depth is around 4 km) that attenuates shorter period (higher frequency) signals.

[11] In the inversion test, synthetic 2-D data (i.e., TE and TM mode data) generated from models in which candidate 3-D melt bodies are superimposed are inverted to evaluate perturbations in the forward modeling responses that are resolvable. The inversion data consist of the synthetic responses at the 12 sites utilized in the forward modeling test and the observed responses at other sites located outside the 12 sites. The observed standard deviations were assigned to the synthetic forward responses, and the observed data scatter was also added to them to ensure compatibility with the real data set. The 2-D inversion program was an advanced nonlinear conjugate gradient algorithm after *Rodi and Mackie* [2001] that incorporates transverse anisotropy. The settings for the synthetic inversions are the same as in *Matsuno et al.* [2010]; the regularization parameter for model smoothness is 1.8, the value for model anisotropy is 100 (i.e., we are seeking an approximately isotropic solution), the horizontal model weighting factor α is 1.0, the model weighting factor β is 1.6, and a priori incorporation of a discontinuity in resistivity at the boundary between the subducted slab and the mantle wedge in the penalty function is included.

[12] Data elements considered in the tests are the TE mode phase and the TM mode apparent resistivity and phase. The TE mode apparent resistivity is not considered because this element was not used by *Matsuno et al.* [2010] (but note that synthetic TE mode apparent resistivity data are shown in some of the figures for reference). The diagonal elements are not considered, but they will be discussed in the context of the sensitivity of a hypothetical 3-D data set to 3-D melt regions in a later section.

[13] The 3-D conductive anomalies superimposed on the background 2-D model to simulate the melt region have a range of shapes, dimensions, and

resistivities. The shapes considered are: rectangular columns; a triangular cross section but elongate along strike; and pyramids (Figure 3). The rectangular column simulates a plausible, if extreme case of buoyant upwelling [e.g., *Scott and Stevenson*, 1989]. The triangle is two dimensional in cross-section but with limited length along strike. A 2-D triangle shape with infinite length along strike simulates a passive melt region beneath the ridge, and has been typical of a faster spreading system [e.g., *Langmuir et al.*, 1992]. The pyramid simulates a melt region with a reasonable degree of melt focused toward the ridge center, and has been postulated for a slower spreading system [e.g., *Parmentier and Phipps Morgan*, 1990]. The dimensions of the melt region are defined by the across-strike (along-transect) length at the bottom of the melt region (hereafter W), the along-strike (across-transect) length at the bottom of the melt region (hereafter L), and the vertical extent. The range of W considered is 15–90 km in increments of 15 km. The values of L investigated are 60 km and 120 km. Smaller values of L (in which L is set equal to W) are also used to simulate a columnar-shaped model inferred from the seismic attenuation structure of *Pozgay et al.* [2009]. The value for L of 60 km is essentially the length of the ridge segment at 18°S within which the MT instruments were deployed, and is also approximately the same as the along-strike dimension of the circular mantle Bouguer anomaly low centered on the segment [*Kitada et al.*, 2006]. The depth to the top of the melt region is fixed at 6 km (the oceanic Moho), and the bottom of the melt region is fixed at ~60 km corresponding to the dry solidus for oceanic mantle. Hydrous melting can be triggered at depths greater than 60 km in the Mariana Trough. The amount of melt produced in the hydrous melt regime is expected to be much lower than that in the anhydrous melt regime above the dry solidus. Accordingly, we first focus on the anhydrous melt region in the forward modeling and inversion tests, and will later briefly discuss the influence of the hydrous melt region on the data.

[14] The postulated resistivities of the melt region are 10, 30, and 100 Ω-m, and are held uniform for simplicity. By setting a uniform resistivity, we are assuming that the interconnected conductive melt is uniformly distributed, and are ignoring the impacts of variations in temperature and pressure in the melt region on the resistivity of melt. The resistivities can be translated to melt fraction based on laboratory models [e.g., *Pommier and Le-Trong*, 2011], as discussed below.

[15] Since MT data are more sensitive to conductance (the product of conductivity and volume) than conductivity within a specific volume, there is a trade-off between the shape parameters, W and L, and the resistivity. For instance, it is possible that two models with different shapes and with different resistivities, but with the same conductance, can have nearly the same MT response. The mean resistivity value in the reference model derived from *Matsuno et al.* [2010] that are replaced with melt anomalies is ~500 Ω-m. Furthermore, note that the present approach assumes that the melt sits in an interconnected network. If this is not true, and melt sits in isolated pockets on grain boundaries, then high melt fractions are possible without impacting the bulk resistivity. However, most studies of melt networks and transport in the mantle suggest fairly good interconnection and rapid removal of melt, indicative of a conductive network even at low melt fractions [e.g., *Kelemen et al.*, 1997; *Faul*, 1997; *Drury and Fitz Gerald*, 1996].

3. Results of Forward Modeling and Inversion Tests

3.1. Forward Modeling Test

[16] For each model considered, pseudosections are constructed that show the difference in MT response of the model under test compared to the reference model, normalized by the error. Examples of such pseudosections are shown in Figures 4 and 5 for models containing a rectangular column, a triangular, and a pyramidal shaped melt region respectively. The resistivity of the melt region shown is 10 Ω-m (Figure 4) and 100 Ω-m (Figure 5), and the W and L values are both 60 km.

[17] With a resistivity of 10 Ω-m for the rectangular column model (Figure 4a), the absolute normalized residuals are >1.0 for almost all of the sites up to periods of ~10^5 s for both the TE and TM modes. The results suggest that a 60 km wide column of melt, continuous along the ridge segment, is inconsistent with the observations. For the triangular shaped model (Figure 4b), the absolute normalized residuals are >1.0 at sites located within 30 km of the ridge and at periods under 10^4 s, indicating that the model is also not consistent with the observations. For the pyramidal model (Figure 4c), the absolute normalized residuals are >1.0 at sites near the model center at periods of $10^3 - 3 \times 10^3$ s in the TM mode, especially in the phase, while the absolute normalized residuals are <1.0 at almost all of
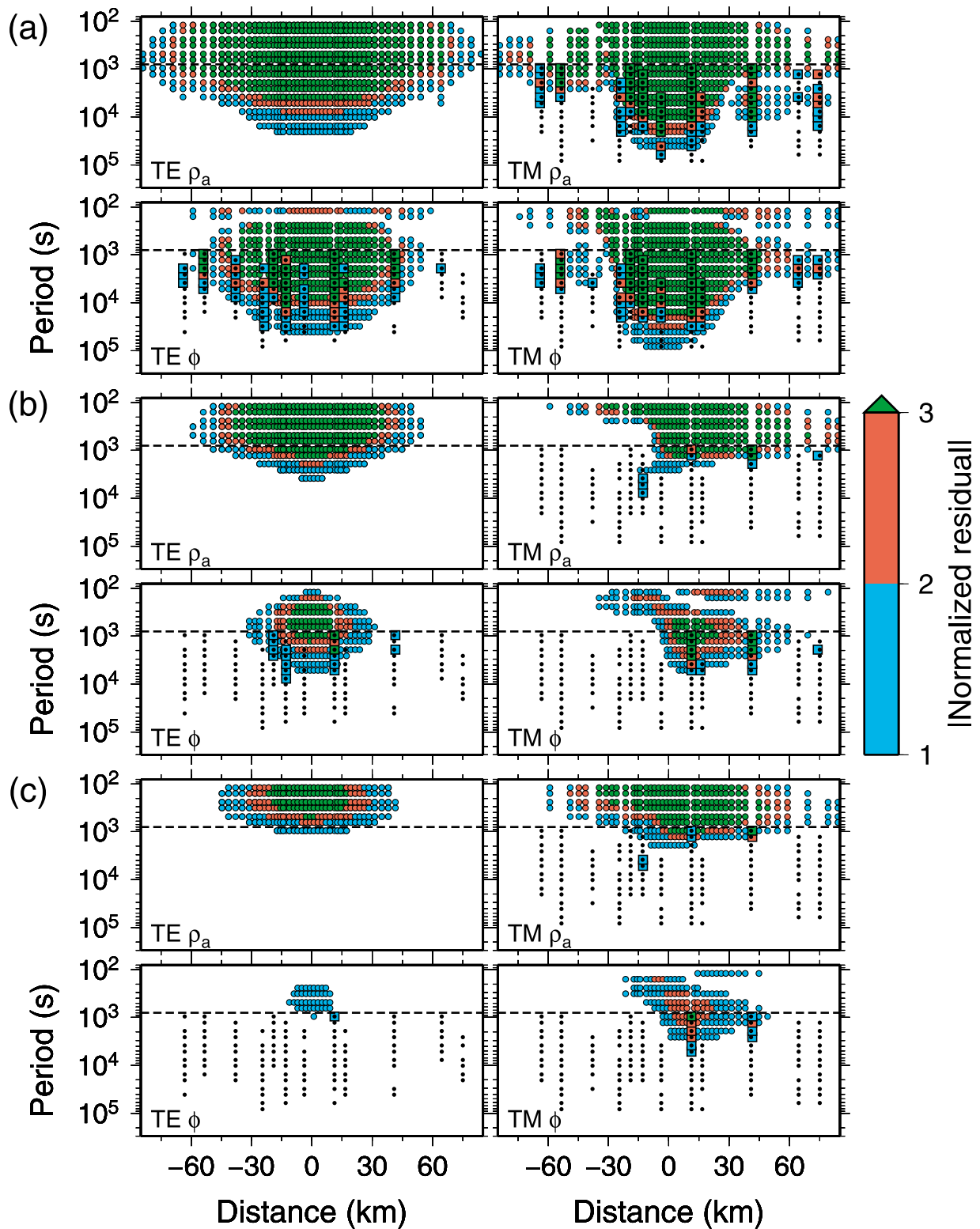
Figure 4. Examples of pseudosections of the absolute normalized residual for three melt region models: (a) rectangular column, (b) triangular, and (c) pyramidal. The resistivity of the melt regions is 10 Ω-m. W (across-strike width) and L (along-strike length) of the melt regions are both 60 km. The color scale shows the normalized residuals between the two synthetic data types. The colors in squares show residuals at actual data points, and those in smaller circles show residuals at hypothetical data points; see text for details. The black dots denote data points used in the 2-D inversions [*Matsuno et al.*, 2010], and the horizontal dashed line in each plot indicates the minimum period of the data set.
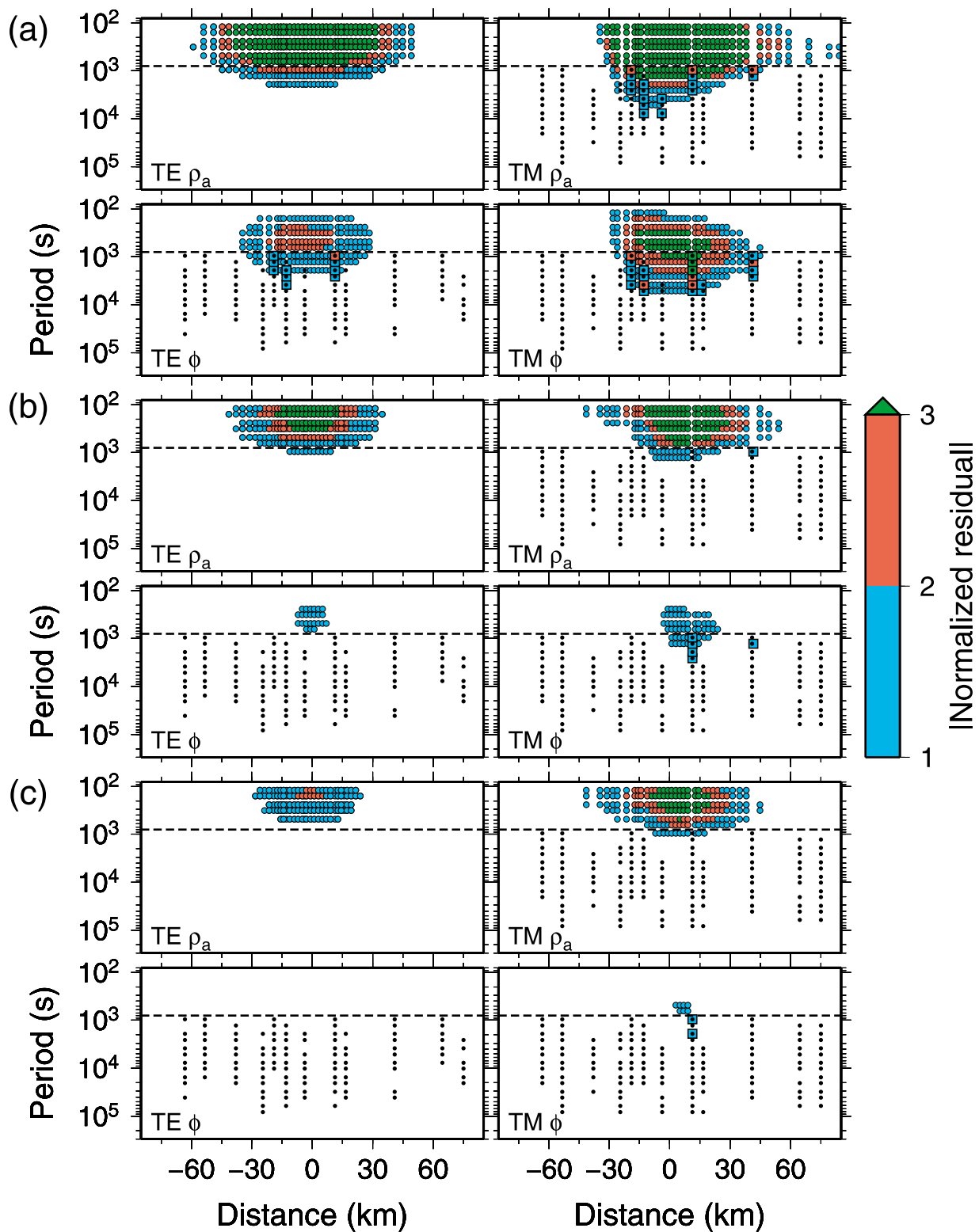
Figure 5. The same as Figure 4 except that the resistivity of the melt regions is 100 Ω-m.

Table 1. Maximum Width (W) in km for the Acceptable Melt Regions for Each Resistivity in Ω-m and for Each Shape of the Melt Region

	Rectangular Column		Triangle		Pyramid	
Resistivity	L = 60	L = 120	L = 60	L = 120	L = 60	L = 120
10	<15	<15	<15	<15	15	<15
30	<15	<15	15	<15	30	15
100	15	15	30–45	30	60–75	30–45

the sites for periods over 10^3 s in the TE mode, indicating that this melt region model is unfeasible.

[18] With a resistivity of 100 Ω-m for the rectangular column model (Figure 5a), absolute normalized residuals >1.0 occur mainly at sites within 30 km of either side of the ridge crest and at periods under 10^4 s. In other words, the area with absolute normalized residuals of >1.0 is smaller for the model with the anomaly of 10 Ω-m (i.e., a higher melt fraction). However, the rectangular column with the dimensions considered is unfeasible for resistivities of both 10 and 100 Ω-m. For the triangular shaped model (Figure 5b), the absolute normalized residuals are >1.0 for only a few values of the TM mode phase near the center of the model (i.e., at the spreading center) at periods of $10^3 - 3 \times 10^3$ s. There are no absolute normalized residuals >1.0 at periods over 10^3 s in the TE mode and in the TM mode apparent resistivity, indicating that this melt region model is more consistent with the observations. For the pyramidal model (Figure 5c), almost all of the absolute normalized residuals are <1.0. The absolute normalized residuals for a few data points are >1.0, but they are scattered, suggesting that this melt region model is feasible. The results for all models considered with L values of 60 and 120 km are tabulated in Table 1. The criterion used to define the allowable model dimensions listed in Table 1 is that the absolute normalized residuals are <1.0. The small changes in conductance between some of the models result in very subtle changes in MT responses leading to multiple acceptable values for the dimensions of the melt region.

[19] We have also considered models with equal values of W and L, and the results are shown in Table 2. The same criterion as used for Table 1 is applied. In this case, acceptable values of W (and L) are slightly larger than the results with L = 60 km, but the differences are insignificant. The results also place a constraint on the maximum along-strike dimension of the melt region.

3.2. Inversion Test

[20] Inversion models using the synthetic forward responses generated from the representative six models of Figures 4 and 5, and the differences between the inversion result and the original 2-D inversion model, are displayed in Figures 6 and 7. The differences between the synthetic models and the original 2-D inversion model that represent superimposed melt bodies are also shown in the same figures. The largest differences between the inversion models and the original 2-D inversion model of >0.5 decade occur around the center of the rectangular column melt region with a resistivity of 10 Ω-m (Figure 6a, middle), and the differences become smaller (<0.5 decade) as the resistivity of the melt region increases and as the shape of the melt region changes from the rectangular column to the triangle, and finally to the pyramid. The differences are smallest (<0.1 decade) for the pyramid melt region with a resistivity of 100 Ω-m (Figure 7c, middle). These variations compare well to the perturbations in the synthetic forward responses shown in Figures 4 and 5. The RMS misfits for the six models are insignificantly different from each other (1.118–1.121 for five models and a smaller value of 1.101 for the rectangular column model with a resistivity of 10 Ω-m), and from the original 2-D inversion model (1.122). RMS misfit and model smoothness curves (L-curves) for inversions using the synthetic data sets and other regularization parameters for model smoothness are quite similar to the curve obtained in the inversion of the original data set. Inversions with other dimensions and resistivities for 3-D melt bodies were also carried out. The model differences in the inversions for the maximum allowable melt bodies listed in Tables 1 and 2 are all <0.1 decade with statistically indistinguishable RMS misfits. Consequently, 3-D melt region models that are concluded to be feasible in the forward modeling test will be difficult to be identified in a 2-D inversion model, while those that are concluded to

Table 2. Maximum Width (W) and Length (L) in km for the Acceptable Melt Regions With Equal W and L for Each Resistivity in Ω-m and for Each Shape of the Melt Region

| Resistivity	Square Column	Triangle	Pyramid
10	<15	15	30
30	15	15	30
100	15	45	60
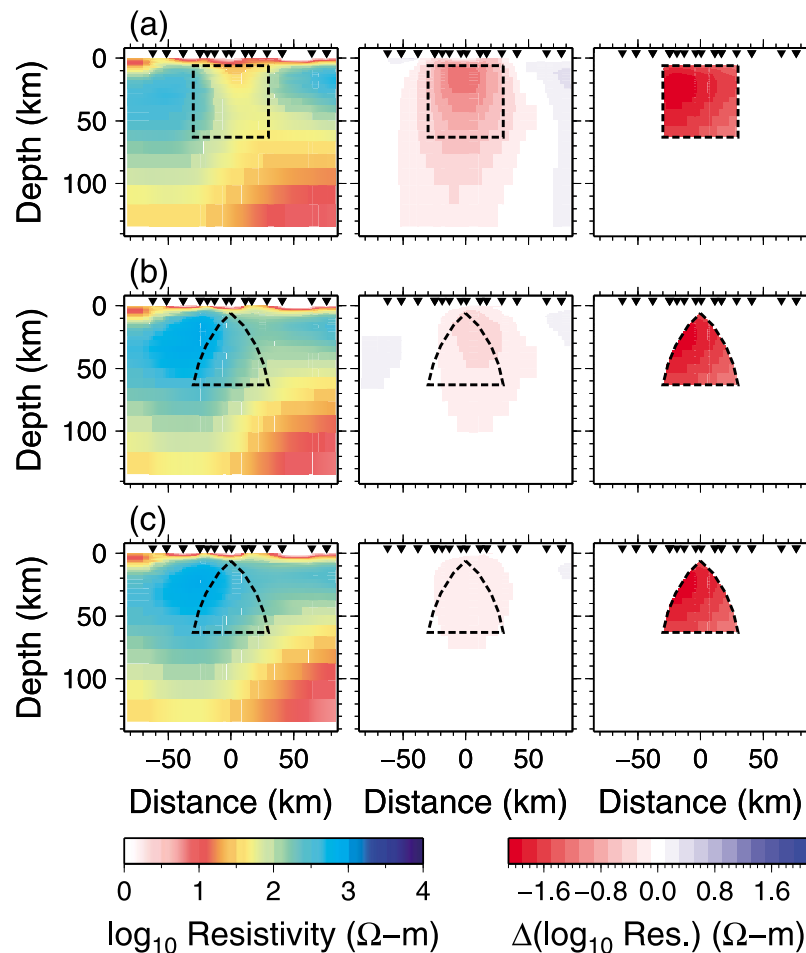
Figure 6. (left) Cross-sections of inversion models using the data generated from synthetic models in which 3-D conductive melt bodies are superimposed on the original 2-D inversion model of *Matsuno et al.* [2010], (middle) the differences between the modified inversion models and the original 2-D inversion model, and (right) the differences between the synthetic 3-D models and the original 2-D inversion model. The model difference is obtained by subtracting the original 2-D model from a model in which the 3-D melt body is superimposed in logarithmic resistivity. The cross-sections cut the center of the superimposed 3-D melt regions. The geometries of the 3-D melt regions are (a) rectangular columnar, (b) triangular, and (c) pyramidal. The dashed lines in each plot delineate the cross-section of each melt region. The geometries of the lines in Figures 6b and 6c appear to be the same, but the actual geometries are 3-D and differ from each other as shown in Figure 3. The resistivity of the melt regions is 10 Ω-m, and W and L are set to 60 km. The color scales are logarithmic, but are different for the models and model differences. The white color in the model differences (both end columns) indicates that absolute values are smaller than 0.1 decade. Inverted filled triangles near the top in each plot indicate station locations used in the inversion.

be unfeasible in the forward modeling test will appear in a 2-D inversion model.

4. Discussion

[21] The forward modeling test have defined the 3-D melt region dimensions, shape and resistivity that are compatible with the measurement errors, and the inversion test have shown that synthetic data derived by superimposing feasible 3-D melt regions on the background model generate very similar

models to those presented in *Matsuno et al.* [2010] with statistically insignificant differences in RMS misfit. The latter implies that the feasible 3-D melt regions will not appear in a 2-D representation of the regional structure. The following discussion covers the melt fractions inferred from resistivity, consistency and inconsistency of the results with other studies, the electromagnetic implications of a melt region and mantle upwelling, and the sensitivity of observed and hypothetical data to possible 3-D melt regions.
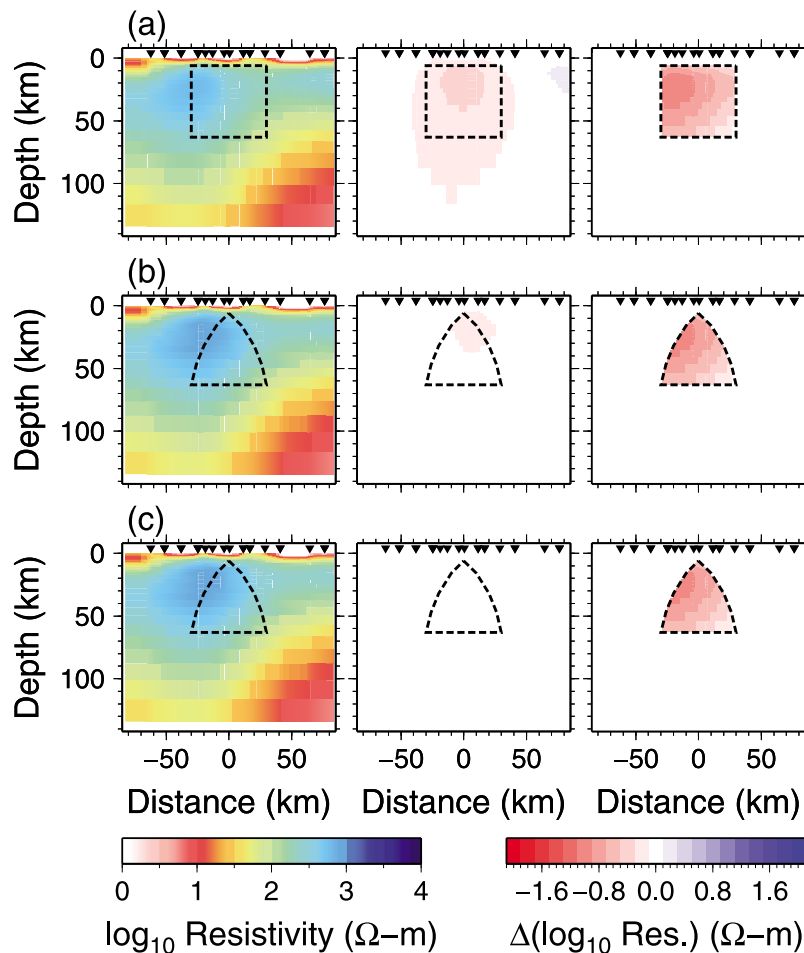
Figure 7. The same as Figure 6 except that the resistivity of the 3-D melt regions is 100 Ω-m.

[22] Regions of anomalously low resistivity seen in MT surveys are often interpreted in terms of an interconnected melt network. Laboratory measurements of the conductivity of melts for a range of compositions and temperature conditions show that silicate melts are ~1–10 S/m (~0.1–1 Ω-m) [e.g., *Roberts and Tyburczy*, 1999; *ten Grotenhuis et al.*, 2005; *Toffelmier and Tyburczy*, 2007; *Yoshino et al.*, 2010; *Pommier and Le-Trong*, 2011]. More critical, however, is the nature of the melt network and the degree of interconnectivity of the melt [e.g., *Schmeling*, 1986; *Roberts and Tyburczy*, 1999; *ten Grotenhuis et al.*, 2005]. We use the Hashin-Shtrikman upper bound, which assumes the end-member case of complete melt connectivity in the host rock [*Hashin and Shtrikman*, 1962] to infer the melt fraction from the resistivity. With the Hashin-Shtrikman upper bound for two phases, if the host resistivity is set at 500 Ω-m, which is the background value found in the 2-D inversion model, and the silicate melt resistivity is set at 10 S/m (0.1 Ω-m) [e.g., *Yoshino et al.*, 2010], then bulk

resistivities of 10, 30, and 100 Ω-m, respectively, correspond to a melt fraction of 1.5%, 0.5%, and 0.1%. Assuming a less conductive melt of 1 S/m [e.g., *Roberts and Tyburczy*, 1999], the corresponding melt fractions are 14%, 4.7%, and 1.2%. Largely as a consequence of the uncertainty about the resistivity of silicate melt, but also because of uncertainties about temperature and melt composition, a wide range of melt fractions are compatible with a given resistivity. If the melt is particularly hydrous and hence more conductive, the melt faction can be even lower [*Ni et al.*, 2011], although very hydrous melts are probably confined to those generated at the slab and transported to the arc.

[23] Seismic attenuation studies suggest a ~75 km wide columnar-shaped melt region in the central Marianas [*Pozgay et al.*, 2009]. However, a narrower melt region remains possible in the attenuation model due to the effect of the smoothing operator used in inversion, although *Pozgay et al.* [2009] did not evaluate the significance of the

width of the high attenuation anomaly in detail. If the melt region contains interconnected melt, the closest model in terms of shape and dimension consistent with the MT data is a pyramidal melt region (W = 60–75 and L = 60) that is fairly resistive (100 Ω-m). The dimensions of this melt region model cover the ∼60 km length of the segment, and as such, is consistent with the along-strike length of a gravity low centered on the segment [*Kitada et al.*, 2006]. An interconnected silicate melt fraction of between 0.1 and 1%, consistent with a resistivity of 100 Ω-m, is broadly compatible with the melt fraction inferred from the seismic attenuation structures by *Pozgay et al.* [2009].

[24] Isolated melt distributed over a length scale of tens of kilometers would not be detected by the Marianas MT data. This could occur if, for example, melt is retained in the mantle away from the primary melt region. That said, the primary melt regions inferred from this study are not wide across- and along-strike, and are considerably smaller than the melt supply region beneath the southern East Pacific Rise [*Baba et al.*, 2006]. The melt region beneath the southern East Pacific Rise is shown to be 2-D extending infinitely along strike, and the minimum melt fraction is ∼1% inferred from a resistivity of ∼10–30 Ω-m for an isotropic model and in the horizontal direction of an anisotropic model, and is >∼4% inferred from a resistivity of <∼10 Ω-m in the vertical direction of the anisotropic model [*Baba et al.*, 2006] (note that the estimation of the minimum melt fraction was based on the parallel bound model for aligned sheets, and was calculated from the resistivity structure, a thermal structure based on a half-space cooling model, and the results of *Xu et al.* [2000] and *Tyburczy and Waff* [1983]). This difference probably reflects a mechanism of buoyant mantle upwelling and focused melt transport at this slow spreading ridge.

[25] The consensus view that melt is focused from a broader melt region at the onset of melting to a narrow melt extraction zone at the seafloor suggests that there is likely to be a small volume with a high melt fraction at depths between 20 and 40 km, as reported by *Kelley et al.* [2010]. To see the effects of such a body, a test was conducted using a model in which a small conductive anomaly of 10 Ω-m extending from the base of the crust down to 25 km depth was added to a uniform resistivity of 100 Ω-m for the triangular and pyramidal models. The results (not shown) suggest that neither model is consistent with the data, but that the effect of including the shallow melt body is larger for the triangular melt

region, suggesting that the pyramidal model is preferred if a high melt fraction area at shallow depth is required on the basis of other data.

[26] The addition of water to the upper mantle can trigger significant hydrous melting below the dry melting regime, and this process is integral to melting processes in subduction zone settings [e.g., *Kelley et al.*, 2006]. Hydration of the mantle lowers the solidus and allows melting to occur at greater depth, typically in excess of 100 km. To test the possibility that hydrous melting is taking place beneath the back-arc ridge, the triangular and pyramidal conductive anomalies (100 Ω-m) were extended to 120 km depth. Absolute residuals with the new models are not changed from those for models without the hydrous melt regions, presumably because the resistivity at these depths is low in the original 2-D inversion models. Such a low resistivity could be due to the existence of melt (or possibly water) in a regional sense under hydrous conditions.

[27] One consideration in understanding the limitations of the data is the band-limited nature of the MT responses. As shown in Figures 4 and 5, the differences in the MT responses for the melt region are large at periods shorter than 10^3 s where the field data are lacking.

[28] Another issue is whether the 2-D transect played a role in limiting the resolving power of the data: could a 3-D grid of stations have done a better job? The sensitivity of data at additional hypothetical 3-D sites was checked through a forward modeling test. Figure 8 shows a plan view of normalized residuals for the off-diagonal elements and apparent resistivity and phase for the diagonal elements at a period of 1280 s for three model shapes having a resistivity of 10 Ω-m. With the x axis oriented along-strike and the y axis oriented across-strike, perturbations in the xy element elongate across-strike, while those in the yx element elongate along-strike. The maximum size of the perturbations in the off-diagonal elements is relatively isotropic. Consequently, 3-D grid data of the off-diagonal elements would not significantly enhance the resolving power to the 3-D melt regions considered. For the diagonal elements, a weak signature in apparent resistivity (<1 Ω-m) is seen at the boundaries of melt regions, especially those with strong three-dimensionality (e.g., the four edges and corners of the rectangular column melt region in Figure 8a), and characteristic patterns in phase are found centered on the melt region. The melt
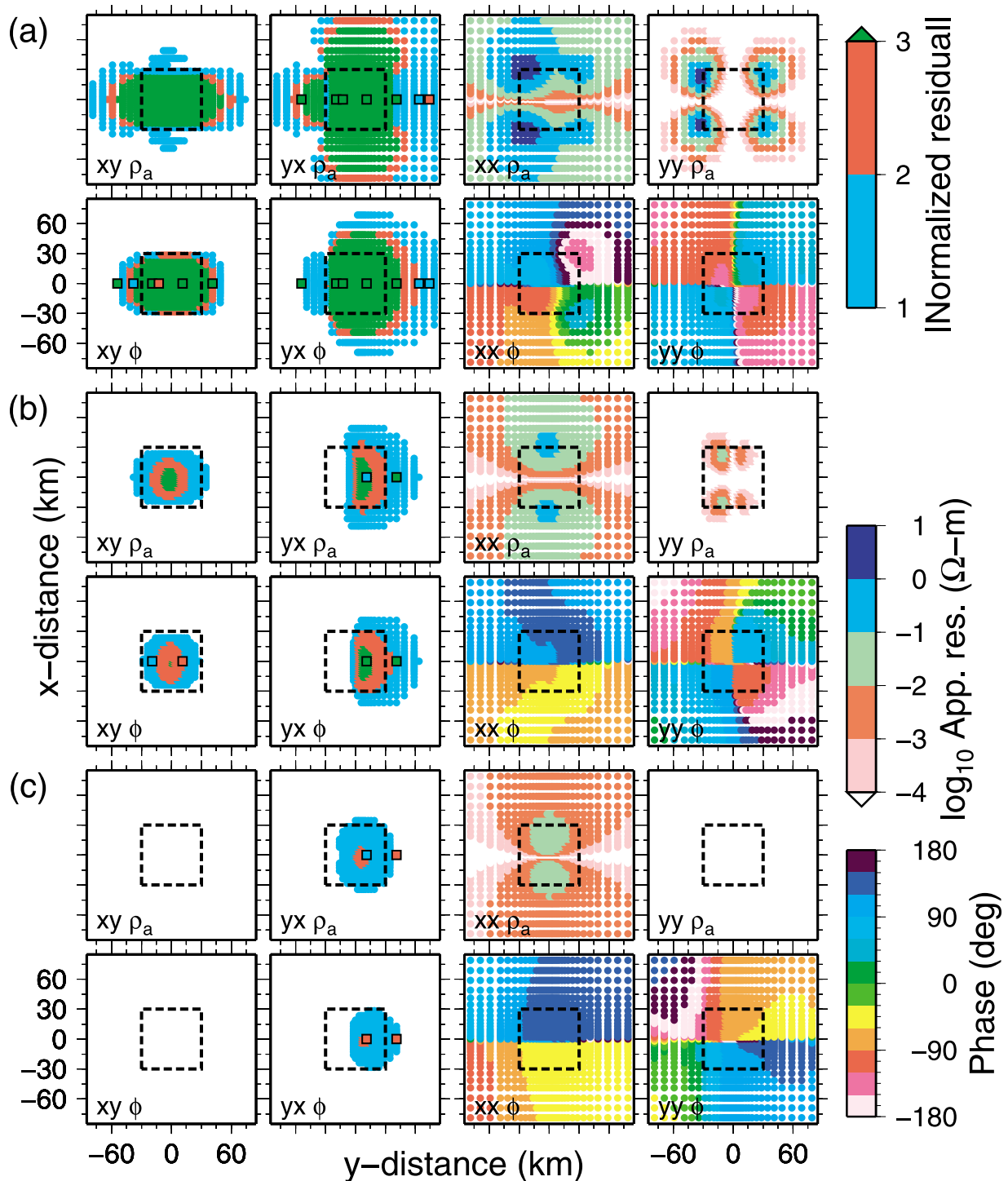
Figure 8. Examples of plan view maps of apparent resistivity and phase at a period of 1280 s for (a) rectangular column, (b) triangular, and (c) pyramidal melt region models. The resistivity of the melt regions is 10 Ω-m. Values plotted for the off-diagonal elements are absolute normalized residuals, while those for the diagonal elements are apparent resistivity and phase. Colors in squares bordered by a black line in the off-diagonal elements indicate the values at the actual data points, and those in circles indicate the values at the hypothetical data points. Dashed squares in the center of each plot delineate a 60 km square outlining the area of the bottom of each melt region model. The actual 2-D transect is located at the 0 km x-distance.

regions tested have sharp edges and corners, while a realistic melt region could have rounder or smoother edges resulting in a conical or elliptical cone shape. Accordingly, the 3-D effects in the modeled MT responses near the edges of the melt region are likely overestimates.

[29] Some of the observed diagonal apparent resistivities are as large as ∼1 Ω-m [*Matsuno et al.*, 2010]. This amplitude is comparable to the synthetic signature near the boundaries of the melt regions off the 2-D transect (Figure 8). Based on the relationship between the location of a 3-D melt region and the resultant distribution of the amplitude of the diagonal apparent resistivity, if a 3-D melt region shifted off the 2-D transect exists, it may generate an amplitude comparable to that observed at sites located on the 2-D transect. In addition, a 3-D melt region offset from the 2-D transect will not generate significant perturbations in the off-diagonal apparent resistivity (Figure 8). Hence, the amplitude of the observed diagonal apparent resistivity may imply the existence of such a 3-D melt region. The circular lows in gravity data found below the target segment and the next one to the south [*Kitada et al.*, 2006] support the existence of a 3-D melt region offset to the south from the 2-D transect. However, 3-D seismic structures inferred from surface waves [*Pyle et al.*, 2010] and body waves [*Barklage*, 2010] did not exhibit clear evidence for such a feature.

[30] Similar modeling for the tipper response showed weak effects, especially at the boundaries of the melt regions, with characteristic patterns corresponding to different geometries of the melt regions. These tipper responses might be useful, but the amplitudes of the synthetic signals are of the same order as the measurement errors. In addition, topographic correction of the marine tipper must be applied with caution because they are strongly dependent on unknown real structure.

5. Conclusion

[31] We have carried out a suite of electromagnetic forward modeling and inversion tests to investigate the feasibility of a 3-D melt region beneath the central Mariana back-arc spreading ridge. We stress that the resistivity model derived from the field data does not require the presence of a 3-D melt region, but we have evaluated whether 3-D melt regions could be compatible with the MT observations. The extent of a possible 3-D melt region in which interconnected silicate melt is retained is not wide

near the Moho, corresponding to a narrow melt extraction zone beneath the center of the ridge. The along-axis dimension of a 3-D melt region in the upper mantle is confined to the segment and broadly consistent with an observed gravity anomaly. If melt exists uniformly at deeper depths, and the melt is focused at shallower points, the 3-D melt region has a pyramidal (or conical) shape, or an intermediate shape between a triangular and pyramidal anomaly. The resistivity of the melt region is 100 Ω-m, against a background resistivity of ∼500 Ω-m, corresponding to an interconnected silicate melt fraction of at most ∼1%, and possibly as small as 0.1%. The maximum allowable melt fraction inferred in the present study is consistent with that from seismic attenuation structure by *Pozgay et al.* [2009]. The lack of a clear conductive anomaly beneath the slow spreading back-arc system, and the limits placed on any feasible 3-D melt body in the region by this study, strongly suggest that melt transport occurs through dynamic buoyancy-driven mechanisms, in contrast to evidence from the fast spreading southern East Pacific Rise.

Acknowledgments

References

Baba, K., and N. Seama (2002), A new technique for the incorporation of seafloor topography in electromagnetic modeling, *Geophys. J. Int.*, *150*(2), 392–402, doi:10.1046/j.1365-246X.2002.01673.x.

Baba, K., A. D. Chave, R. L. Evans, G. Hirth, and R. L. Mackie (2006), Mantle dynamics beneath the East Pacific Rise at 17°S: Insights from the Mantle Electromagnetic and Tomography (MELT) experiment, *J. Geophys. Res.*, *111*, B02101, doi:10.1029/2004JB003598.

Barklage, M. (2010), Structure and seismicity of the upper mantle using deployments of broadband seismographs in Antarctica and the Mariana Islands, PhD thesis, 116 pp., Washington Univ., St. Louis, Mo.

Bibee, L. D., G. G. Shor Jr., and R. S. Lu (1980), Inter-arc spreading in the Mariana Trough, *Mar. Geol.*, *35*, 183–197, doi:10.1016/0025-3227(80)90030-4.

Drury, M. R., and J. D. Fitz Gerald (1996), Grain boundary melt films in an experimentally deformed olivine-orthopyroxene rock: Implications for melt distribution in upper mantle rocks, *Geophys. Res. Lett.*, *23*(7), 701–704, doi:10.1029/96GL00702.

Dunn, R. A., V. Lekić, R. S. Detrick, and D. R. Toomey (2005), Three-dimensional seismic structure of the Mid-Atlantic Ridge (35°N): Evidence for focused melt supply and lower crustal dike injection, *J. Geophys. Res.*, *110*, B09101, doi:10.1029/2004JB003473.

Faul, U. H. (1997), Permeability of partially molten upper mantle rocks from experiments and percolation theory, *J. Geophys. Res.*, *102*, 10,299–10,311, doi:10.1029/96JB03460.

Forsyth, D. W. (1996), Partial melting beneath a Mid-Atlantic Ridge Segment detected by teleseismic PKP delays, *Geophys. Res. Lett.*, *23*(5), 463–466, doi:10.1029/96GL00379.

Hashin, Z., and S. Shtrikman (1962), A variational approach to the theory of the effective magnetic permeability of multiphase materials, *J. Appl. Phys.*, *33*, 3125–3131, doi:10.1063/1.1728579.

Hawkins, J. W., P. F. Lonsdale, J. D. Macdougall, and A. M. Volpe (1990), Petrology of the axial ridge of the Mariana Trough backarc spreading center, *Earth Planet. Sci. Lett.*, *100*, 226–250, doi:10.1016/0012-821X(90)90187-3.

Heinson, G., S. Constable, and A. White (2000), Episodic melt transport at mid-ocean ridges inferred from magnetotelluric sounding, *Geophys. Res. Lett.*, *27*(15), 2317–2320, doi:10.1029/2000GL011473.

Hussong, D. M., and S. Uyeda (1982), Tectonic processes and the history of the Mariana arc: A synthesis of the results of Deep Sea Drilling Project Leg 60, *Initial Rep. Deep Sea Drill. Proj.*, *60*, 909–929.

Kato, T., J. Beavan, T. Matsushima, Y. Kotake, J. T. Camacho, and S. Nakao (2003), Geodetic evidence of back-arc spreading in the Mariana Trough, *Geophys. Res. Lett.*, *30*(12), 1625, doi:10.1029/2002GL016757.

Kelemen, P. B., G. Hirth, N. Shimizu, M. Spiegelman, and H. J. B. Dick (1997), A review of melt migration processes in the adiabatically upwelling mantle beneath oceanic spreading ridges, *Philos. Trans. R. Soc. London, Ser. A*, *355*, 283–318, doi:10.1098/rsta.1997.0010.

Kelley, K. A., T. Plank, T. L. Grove, E. M. Stolper, S. Newman, and E. Hauri (2006), Mantle melting as a function of water content beneath back-arc basins, *J. Geophys. Res.*, *111*, B09208, doi:10.1029/2005JB003732.

Kelley, K. A., T. Plank, S. Newman, E. M. Stolper, T. L. Grove, S. Parman, and E. H. Hauri (2010), Mantle melting as a function of water content beneath the Mariana arc, *J. Petrol.*, *51*, 1711–1738, doi:10.1093/petrology/egq036.

Kitada, K., N. Seama, T. Yamazaki, Y. Nogi, and K. Suyehiro (2006), Distinct regional differences in crustal thickness along the axis of the Mariana Trough, inferred from gravity anomalies, *Geochem. Geophys. Geosyst.*, *7*, Q04011, doi:10.1029/2005GC001119.

Langmuir, C., E. Klein, and T. Plank (1992), Petrological systematics of mid-ocean ridge basalts: Constraints on melt generation beneath ocean ridges, in *Mantle Flow and Melt Generation Beneath Mid-Ocean Ridges*, *Geophys. Monogr. Ser.*, vol. 71, edited by J. Phipps Morgan, D. K. Blackman, and J. M. Sinton, pp. 183–280, AGU, Washington, D. C., doi:10.1029/GM071p0183.

Lin, J., G. M. Purdy, H. Schouten, J.-C. Sempere, and C. Zervas (1990), Evidence from gravity data for focused magmatic accretion along the Mid-Atlantic Ridge, *Nature*, *344*, 627–632, doi:10.1038/344627a0.

MacGregor, L. M., S. Constable, and M. C. Sinha (1998), The RAMESSES experiment—III. Controlled-source electromagnetic sounding of the Reykjanes Ridge at 57°45′N, *Geophys. J. Int.*, *135*, 773–789, doi:10.1046/j.1365-246X.1998.00705.x.

Magde, L. S., D. W. Sparks, and R. S. Detrick (1997), The relationship between buoyant mantle flow, melt migration, and gravity bull's eyes at the Mid-Atlantic Ridge between 33°N and 35°N, *Earth Planet. Sci. Lett.*, *148*, 59–67, doi:10.1016/S0012-821X(97)00039-3.

Matsuno, T., et al. (2010), Upper mantle electrical resistivity structure beneath the central Mariana subduction system, *Geochem. Geophys. Geosyst.*, *11*, Q09003, doi:10.1029/2010GC003101.

Ni, H., H. Keppler, and H. Behrens (2011), Electrical conductivity of hydrous basaltic melts: Implications for partial melting in the upper mantle, *Contrib. Mineral. Petrol.*, *162*, 637–650, doi:10.1007/s00410-011-0617-4.

Parmentier, E. M., and J. Phipps Morgan (1990), Spreading rate dependence of three-dimensional structure in oceanic spreading centres, *Nature*, *348*, 325–328, doi:10.1038/348325a0.

Pearce, J. A., and R. J. Stern (2006), The origin of back-arc basin magmas: Trace element and isotopic perspectives, in *Back-Arc Spreading Systems: Geological, Biological, Chemical, and Physical Interactions*, *Geophys. Monogr. Ser.*, vol. 166, edited by D. M. Christie et al., pp. 63–86, AGU, Washington, D. C., doi:10.1029/166GM06.

Pearce, J. A., R. J. Stern, S. H. Bloomer, and P. Fryer (2005), Geochemical mapping of the Mariana arc-basin system: Implications for the nature and distribution of subduction components, *Geochem. Geophys. Geosyst.*, *6*, Q07006, doi:10.1029/2004GC000895.

Pommier, A., and E. Le-Trong (2011), "SIGMELTS": A web portal for electrical conductivity calculations in geosciences, *Comput. Geosci.*, *37*, 1450–1459, doi:10.1016/j.cageo.2011.01.002.

Pozgay, S. H., D. A. Wiens, J. A. Conder, H. Shiobara, and H. Sugioka (2009), Seismic attenuation tomography of the Mariana subduction system: Implications for thermal structure, volatile distribution, and slow spreading dynamics, *Geochem. Geophys. Geosyst.*, *10*, Q04X05, doi:10.1029/2008GC002313.

Pyle, M. L., D. A. Wiens, D. S. Weeraratne, P. J. Shore, H. Shiobara, and H. Sugioka (2010), Shear velocity structure of the Mariana mantle wedge from Rayleigh wave phase velocities, *J. Geophys. Res.*, *115*, B11304, doi:10.1029/2009JB006976.

Roberts, J., and J. Tyburczy (1999), Partial-melt electrical conductivity: Influence of melt composition, *J. Geophys. Res.*, *104*(B4), 7055–7065, doi:10.1029/1998JB900111.

Rodi, W., and R. L. Mackie (2001), Nonlinear conjugate gradients algorithm for 2-D magnetotelluric inversion, *Geophysics*, *66*, 174–187, doi:10.1190/1.1444893.

Schmeling, H. (1986), Numerical models on the influence of partial melt on elastic, anelastic and electrical properties of rocks. Part II: Electrical conductivity, *Phys. Earth Planet. Inter.*, *43*, 123–136, doi:10.1016/0031-9201(86)90080-4.

Scott, D. R., and D. J. Stevenson (1989), A self-consistent model of melting, magma migration and buoyancy-driven circulation beneath mid-ocean ridges, *J. Geophys. Res.*, *94*(B3), 2973–2988, doi:10.1029/JB094iB03p02973.

Seama, N., K. Baba, H. Utada, H. Toh, N. Tada, M. Ichiki, and T. Matsuno (2007), 1-D electrical conductivity structure beneath the Philippine Sea: Results from an ocean bottom magnetotelluric survey, *Phys. Earth Planet. Inter.*, *162*, 2–12, doi:10.1016/j.pepi.2007.02.014.

Stolper, E., and S. Newman (1994), The role of water in the petrogenesis of Mariana trough magmas, *Earth Planet. Sci. Lett.*, *121*, 293–325, doi:10.1016/0012-821X(94)90074-4.

Takahashi, N., S. Kodaira, Y. Tatsumi, Y. Kaneda, and K. Suyehiro (2008), Structure and growth of the Izu-Bonin-Mariana arc crust: 1. Seismic constraint on crust and mantle structure of the Mariana arc–back-arc system, *J. Geophys. Res.*, *113*, B01104, doi:10.1029/2007JB005120.

ten Grotenhuis, S. M., M. R. Drury, C. J. Spiers, and C. J. Peach (2005), Melt distribution in olivine rocks based on electrical conductivity measurements, *J. Geophys. Res.*, *110*, B12201, doi:10.1029/2004JB003462.

Toffelmier, D. A., and J. A. Tyburczy (2007), Electromagnetic detection of a 410-km-deep melt layer in the southwestern United States, *Nature*, *447*, 991–994, doi:10.1038/nature05922.

Tyburczy, J. A., and H. S. Waff (1983), Electrical conductivity of molten basalt and andesite to 25 kilobars pressure: Geophysical significance and implications for charge transport and melt structure, *J. Geophys. Res.*, *88*(B3), 2413–2430, doi:10.1029/JB088iB03p02413.

Wessel, P., and W. H. F. Smith (1998), New, improved version of the Generic Mapping Tools released, *Eos Trans. AGU*, *79*, 579, doi:10.1029/98EO00426.

Xu, Y., T. J. Shankland, and B. T. Poe (2000), Laboratory-based electrical conductivity in the Earth's mantle, *J. Geophys. Res.*, *105*(B12), 27,865–27,875, doi:10.1029/2000JB900299.

Yoshino, T., M. Laumonier, E. McIsaac, and T. Katsura (2010), Electrical conductivity of basaltic and carbonatite melt-bearing peridotites at high pressures: Implications for melt distribution and melt fraction in the upper mantle, *Earth Planet. Sci. Lett.*, *295*, 593–602, doi:10.1016/j.epsl.2010.04.050.